



Vertically aligned carbon nanotube electrodes for high current density operating proton exchange membrane fuel cells



Shigeaki Murata*, Masahiro Imanishi, Shigeki Hasegawa, Ryoichi Namba

Toyota Motor Corporation, Fuel Cell System Development Div., R&D Group, 1, Toyota-cho, Toyota, Aichi 471-8571, Japan

HIGHLIGHTS

- Electrodes for PEMFCs were prepared using vertically aligned carbon nanotubes (CNTs).
- The electrodes enabled high performance (2.6 A cm^{-2}) with low Pt loading (0.1 mg cm^{-2}).
- The wavy CNTs did not make agglomeration during the wet manufacturing process.
- Vertically aligning was important for manufacturing but was irrelevant for performance.

ARTICLE INFO

Article history:

Received 6 August 2013

Received in revised form

14 November 2013

Accepted 19 November 2013

Available online 10 December 2013

Keywords:

High current density

Carbon nanotube

Vertical align

Mass transport

Agglomerate

Fuel cells

ABSTRACT

We successfully developed cathode electrodes for polymer electrolyte membrane fuel cells (PEMFC) that enable operation at high current densities by incorporating vertically aligned carbon nanotubes (CNTs) as the catalyst support; additionally, we prepared 236 cm^2 membrane electrodes assemblies (MEAs) for vehicular use. The electrode structure improved the mass transport of reactants, i.e. oxygen, proton, electron and water, in systems performing at a 2.6 A cm^{-2} current density and 0.6 V with extremely low platinum (Pt) loading at the cathode (0.1 mg cm^{-2}). The improved mass transport caused the 70 mV dec^{-1} Tafel slope to continue up to 1.0 A cm^{-2} . The mass transport was improved because the pores were continuous, the catalyst support materials did not agglomerate and the catalyst layer made good electrical contact with the microporous layer. Utilizing wavy coil-shaped CNTs was also crucial. These CNTs displayed anti-agglomerative characteristics during the wet manufacturing process and maintained a continuous pore structure framing the layered catalyst structure. Because the CNTs had elastic characteristics, they might fill the space between catalyst and microporous layers to prevent flooding. However, the compressed CNTs in the cells were no longer vertically aligned. Therefore, vertically aligning the nanotubes was important during the MEA manufacturing process but was irrelevant for cell performance.

© 2013 Elsevier B.V. All rights reserved.

1. Introduction

Proton exchange membrane fuel cells (PEMFCs) may be used as zero emission power sources for automobiles that utilize hydrogen gas produced from renewable energy sources. The widespread use of PEMFCs depends on their performance, durability and expense [1]. Reducing the use of precious metals and other fuel cell stack components, such as membrane, gas diffusion layer (GDL), separator and others, is critical to reduce costs. To increase the power density and downsize the stacks, the overpotentials must be reduced. The largest well-known activation overpotential arises

from the cathode undergoing oxygen reduction reactions (ORR) when operating under high current density (over 2 A cm^{-2}); additionally the ohmic resistance, mass transport overpotential and the electro-osmotic dehydration of the anode must be considered [2,3].

The mass transfer overpotential in the catalyst layer account for 20–50% of the total mass transfer overpotential [2,4]. To improve the mass transport in catalyst layer, various approaches to control the catalyst layer's structure have included using new materials and/or changing the catalyst layer fabrication process; fabrication processes generally follow the ink-based process developed by the Los Alamos National Laboratory (LANL) team in the early 1990s [5–10]. For this purpose, two approaches exist: one is ultrathin electrodes [6,10] and the other is structural control [7–9]. CNT-based catalyst layers, which are classified into second approach,

* Corresponding author. Tel.: +81 565 72 9145; fax: +81 565 72 9209.

E-mail addresses: shigeaki_murata@mail.toyota.co.jp, sige.m@vc.tnc.ne.jp (S. Murata).

are widely reported because they have unique properties [11–15], such as durability against high potential oxidation due to its graphitic lattice [16–18], improved platinum (Pt) particle activity caused by the support [19–22] and elastic nanotubes [23]. Due to these unique characteristics, we have developed electrodes based on vertically aligned CNTs (VACNTs) over the last ten years [18,24,25]. The vertically aligned structure enhances the gas diffusivity, water drainage and effective utilization of Pt (Fig. 1).

Utilizing VACNTs in PEMFC-electrodes remains challenging due to bundle formation (agglomeration). VACNTs make bundles very easily [26], and there are two main strategies to avoid CNT bundling. One method involves using only dry fabrication processes [27], and the other requires the development of anti-bundling wet processes. Choosing the second strategy, we developed VACNTs with structures resistant to bundling and selected appropriate fabrication solutions and drying methods. When the simple geometrically shaped VACNTs electrodes are complete, the effects of their characteristics, such as thickness, pore volume ratio or ionomer carbon ratio, on cell performance might be experimentally analyzed and evaluated.

2. Experimental

2.1. Preparation of MEAs

Fig. 2 illustrates the sample preparation process. The VACNTs were grown on a stainless steel substrate coated with iron catalysts and an inactive oxide, such as alumina, by the chemical vapor deposition method [28] developed by the Hitachi Zosen Corporation [29,30]. Details about the CNTs are listed in Table 1. Two parameters are important during the VACNTs fabrication process, i.e., the adequate number density and high tortuosity defined by dividing the length of CNTs by the height of VACNT forest. There are two types of VACNTs, one is constituted by tortuous and sparse CNTs, applied in this report shown in Fig. 3, and another is constituted by straight and dense CNTs, cf. supporting online material of reference [23]. The number density of our CNTs was measured to be 3×10^9 tubes cm^{-2} by cross-sectional TEM observations, and the tortuosity τ was estimated using the following equation,

$$m_{\text{CNT}} = \frac{\pi}{4} d^2 h \tau n \rho_{\text{CNT}} \quad (1)$$

where m_{CNT} is the CNT weight per area of the substrate, d , h , n and ρ_{CNT} are the diameter, height, number density and density of the

CNTs, respectively (for ρ_{CNT} , 2 g cm^{-3} was used assuming same as that of carbon). The tortuosity was estimated to be about 2, being not so far from the impression of TEM observation result in Fig. 3. Highly tortuous CNTs avoid bundling, and adequate number density allows solution impregnation. The diameters of the ionomer colloids in solution are usually between hundreds and thousands of nanometers [31,32]; for the dense VACNT forests, the ionomer colloids were filtered on top of the CNTs and could not cover the surface of middle to bottom of CNTs during our experiments, influencing the cell performance.

Subsequently Pt deposition (2 and 3 in Fig. 2) was conducted using a conventional impregnation-dry- H_2 reduction method. $\text{Pt}(\text{NO}_2)_2(\text{NH}_3)_2$ was selected as the Pt source and the solution was transferred from nitric acid to a low surface tension solution ethanol [33] to prevent the CNTs from bundling. The Pt loading was 0.1 mg cm^{-2} . Fig. 4 shows the TEM image of the Pt deposited CNTs. The diameter of the Pt particles were about 2–2.5 nm.

Next, an ionomer dipping process was used to coat the Pt on the CNTs with ionomers (4 and 5 in Fig. 2). The ionomer was not Nafion DE2020, but a newly-developed perfluorosulfonic acid polymer. Additionally, during this process, the solutions' water content was decreased below 2%, preventing the CNTs from bundling. The ionomer to CNTs weight ratio was controlled and reached 1.5. As mentioned above, in this process the ionomer is passing through CNT forest similar to filtration process. The ionomer colloids would be subjected to a shear stress and broken into smaller colloid particles. It could be assumed they would not make aggregations and uniformly cover the CNTs.

Finally, for the MEA fabrication process (6 in Fig. 2), the catalyst layer on the substrate was decal-transferred to a $10 \mu\text{m}$ thick, reinforced perfluorosulfonic acid membrane. The substrate was hot-pressed at 140°C under 5 MPa for 10 min before the substrate was peeled off. The anode catalyst layer was fabricated using a conventional spray method ink process using a 30 wt.% Pt/Ketjen catalysts (Tanaka Kikinzoku, TEC10E30E). The Pt loading of the anode was 0.05 mg cm^{-2} and the ionomer to carbon weight ratio was 1.0. These MEAs were assembled in cells after hot pressing with GDLs. The thickness of the VACNT electrodes was optimized for cell performance by controlling the assembly pressure and/or clearance, generating cells approximately $8 \mu\text{m}$ thick.

MEAs were fabricated in three sizes: 1 cm^2 , 20 cm^2 and 236 cm^2 . The details of MEA fabrication are listed in Table 2. MEAs using conventional electrodes were also prepared as reference materials. The differences between the experimental and reference materials are the catalyst support and the cathodic ionomer carbon weight ratio (I/C), as illustrated in Table 2.

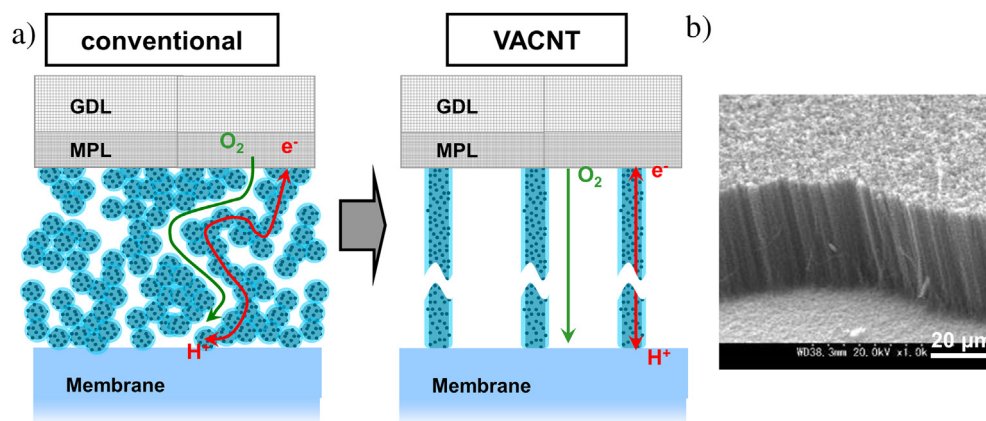


Fig. 1. a) Concept of VACNT electrodes, b) SEM Image of VACNTs.

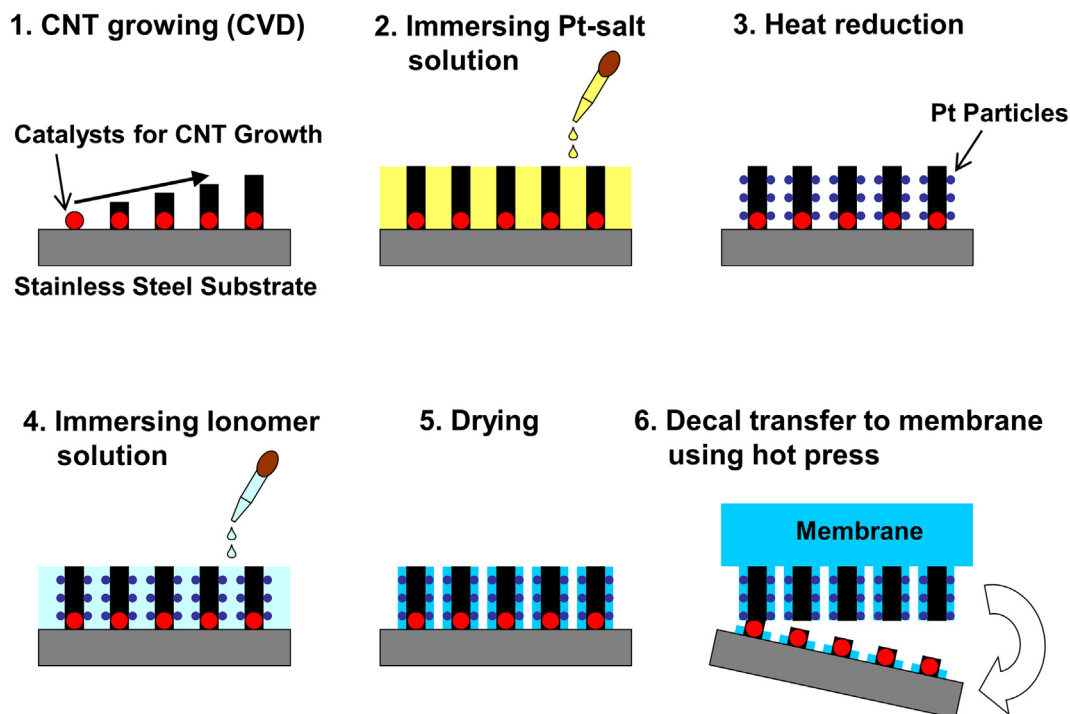


Fig. 2. Preparation procedure of VACNT electrodes MEA.

2.2. Electrochemical properties

2.2.1. Rotating disc electrode (RDE) test

We evaluated the catalytic activity of the CNT-supported Pt particles with the rotating disc electrode (RDE) method. Pt/CNT samples were scraped from the substrate after step No. 3 in Fig. 2, dispersed in ionomer-containing solution (0.025 wt.% in water and isopropanol) and adhered to a glassy carbon RDE. The 1.65 μg Pt loading on the RDE was confirmed by ICP. All RDE measurements were conducted at 25 °C in a 0.1 M perchloric acid electrolyte solution while rotating at 1600 rpm. After 20 cycles of cyclic voltammetry (CV) sweeps within 0.05–1.2 V vs. RHE in an argon-saturated solution, CV was measured to obtain the electrochemical surface area (ECSA) in the same cell. Catalytic activity was obtained using a linear sweep voltammetry (LSV) measurement in an oxygen-saturated 0.1 M perchloric solution within 0.05–1.05 V vs. RHE at 10 mV s^{-1} . A conventional Pt on carbon catalyst (TEC10E30E, same catalyst used for the reference MEA) was used as a reference. The reference samples for the RDE measurements were all prepared in the same way, and the 3.19 μg Pt loading on the RDE was confirmed.

2.2.2. Single cell performance

Our original 20 cm^2 cells were designed to mimic our original 236 cm^2 cell. The length of the flow field, the opposing air and

hydrogen flow directions, and the flow pattern generated by the porous metal foam materials were kept constant between the 20 cm^2 and 236 cm^2 cells to conduct fuel cell performance tests using smaller cells under analogous testing conditions. Using these two cells, IV performance tests were conducted using our standard operating conditions simulating use during vehicle operation. The cell performance properties were measured relative to the operating temperature (temperature characteristics test) to evaluate the robustness against drying and flooding in the 20 cm^2 cell. The cell temperature was increased from 60 °C to 85 °C in 5 °C increments and in 1–2 °C increments up to 110 °C under a constant 1 A cm^{-2} current without gas humidification. The gas diffusivity was evaluated by measuring the limited current density with 1% O_2/N_2 gas at the cathode with a 1 cm^2 cell (Oxygen transport resistance measurement) [34]. The test conditions are summarized in Table 3.

2.2.3. Durability

A 20 cm^2 cell was used during the durability test, and the test conditions are summarized in Table 4. To focus on Pt dissolution and mitigate the influence of carbon corrosion, the steps in potential were set in the relatively high potential range between 0.60 V and 0.90 V, while being kept for 5 s at each step. The gas species, humidity and pressure were analogous to the Fuel Cell Commercialization Conference of Japan's (FCCJ) test protocol [35]; however, the cell temperature and upper voltage of the potential steps were lower, eliminating the effects of carbon corrosion but requiring many hours to complete the tests.

2.3. Characterization/morphology observation

2.3.1. SEM

The cross-sectional images of the cathode catalyst layer were obtained with a FE-SEM (HITACHI S-4700, Acceleration voltage: 5 kV). To obtain cross-sectional images of the catalyst layer, the test

Table 1
Specifications of VACNTs.

Type of CNTs	Multi-walled CNTs
Length	40–60 μm
Tortuosity	2
Diameter	20 nm
Number density	3×10^9 tubes cm^{-2}
Average distance	200 nm
Weight	0.2 mg cm^{-2}
Specific surface area	200 $\text{m}^2 \text{g}^{-1}$

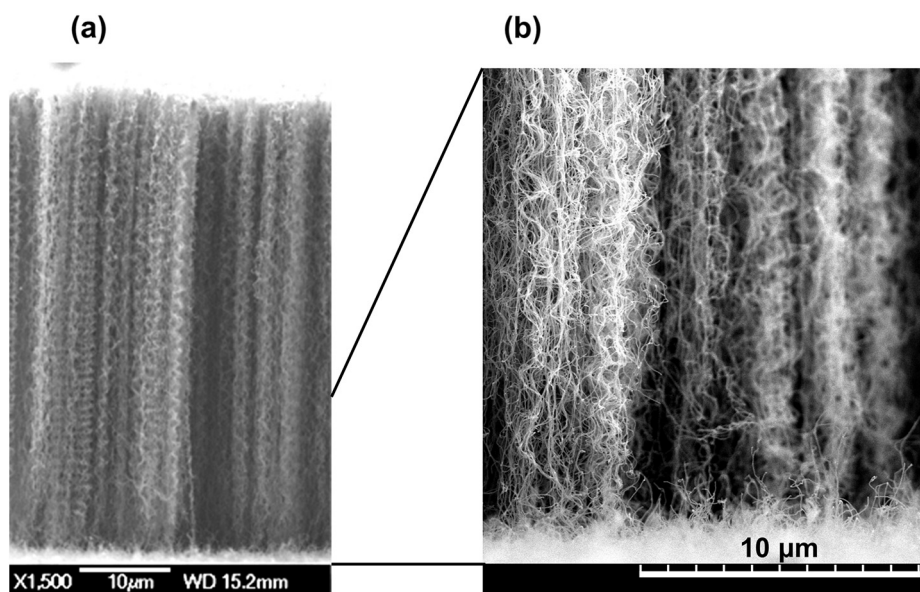


Fig. 3. High resolution SEM image of VACNTs.

cell was impregnated with sublimed material to preserve the microstructure during cross sectioning by focused ion beam micromachining. The sublimed material was removed before the SEM images were taken. The components' volume fractions and the pores in the catalyst layer were estimated using the catalyst layer thickness measured using this SEM image, in addition to the catalyst layer components' weight and density (CNTs or carbon black, ionomer and Pt).

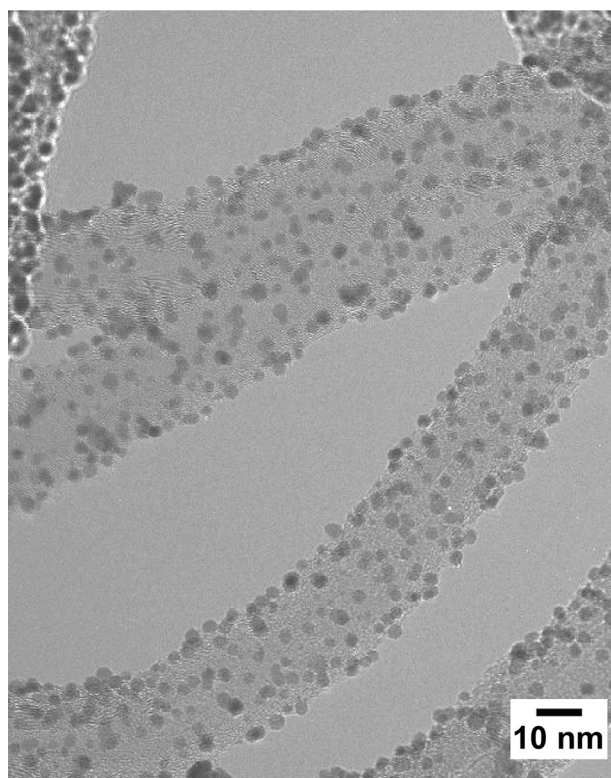


Fig. 4. TEM image of Pt particles on CNTs.

2.3.2. Compression properties

We evaluated the compression characteristics of the cathode catalyst layer using two methods. The first was a general stress-strain parameter measurement. For the measurements, VACNT electrode transferred membranes (same as step 6 of Fig. 2) were used as samples. Test setup is illustrated in Fig. 5. The second was in-situ observation using SEM. VACNTs on Si substrate were placed on the SEM stage after impregnation with ionomer (same as step 5 of Fig. 2 except for the substrate material). Piezoelectric elements were connected in series to gain enough strokes before being used to compress the CNTs, as presented in Fig. 6.

3. Results and discussion

3.1. Electrochemical properties

The fuel cells' IV performance data are displayed in Fig. 7. IV performances obtained using the 20 cm² cell and 236 cm² cells were identical. In Fig. 7, the cell resistance was measured using the current interrupt method; the IR-corrected IV performance data for 20 cm² cell were also plotted. The IV performances obtained from these cells were 2.6 A cm⁻² at 0.6 V; the power output per Pt unit mass was 10.4 kW g⁻¹. Because the US-DOE's 2017 target is 8 kW g⁻¹_{PGM} (PGM: Platinum Group Metal) [36], our proposed CNT-based MEA exceeds performance necessary to overcome this target.

Fig. 8 displays the RDE measurement results. The kinetic current densities were found by fitting Eq. (2), combination of Tafel

Table 2
Specifications of electrode and MEA.

	VACNT electrodes	Conventional electrodes
Pt loading	0.1 mg cm ⁻²	←
Pt particle size	2–2.5 nm	←
Catalyst support	MWCNT	Ketjen black
Catalyst support weight	0.2 mg cm ⁻²	←
I/C	1.5	0.75
Thickness	8 μm (in cell)	←
Porosity	0.65	←
Anode Pt loading	0.05 mg cm ⁻²	←
Membrane	10 μm	←

Table 3
Test conditions for single cell performance tests.

<i>I–V performance test</i>	
Cell temperature	65 °C
St ratio at anode	1.25–2.2
St ratio at cathode	1.5–2
Gas pressure (inlet of anode)	120–50 kPa gauge
Gas pressure (outlet of cathode)	40–0 kPa gauge
Dew point	Anode 45 °C Cathode dry
Measuring sequence	High to low current, 15 min for every point
<i>Temperature characteristics test</i>	
Current density	1 A cm ^{−2}
Cell temperature	60 °C to UP
St. ratio at anode	1.2
St. ratio at cathode	1.3
Gas pressure (inlet of anode)	140 kPa gauge
Gas pressure (outlet of cathode)	170 kPa gauge
Dew point	AN 45 °C, CA Dry
Measuring sequence	Low to high temperature, 15 min for every point
<i>Oxygen transport resistance measurement test</i>	
Cell temperature	80 °C
Anode gas	H ₂ , 500 Nm L min ^{−1} , RH 80%
Cathode gas	1% O ₂ /N ₂ (dry base), 1000 Nm L min ^{−1} , RH 80%
Gas pressure	50 kPa gauge

equation and Koutecky–Levich equation, to the cathodic sweep data in Fig. 8(a), where a and b are Tafel constants, i_k is the kinetic current density, i_L is limiting current density and i is the observed current density [37,38].

$$E = a - b \log i_k = a - b \log \left(\frac{i_L i}{i_L - i} \right) \quad (2)$$

The mass activity (MA) was defined by dividing the kinetic current density at 0.9 V vs. RHE by the mass of Pt loaded on the RDE. The MA of the Pt particles on the CNT (Pt/CNT) was 316 A g^{−1}_{Pt}, while the MA of the conventional Pt/C catalyst was 203 A g^{−1}_{Pt}, and the Tafel slope b were both 70 mV dec^{−1} ECSAs, obtained from the charge of hydrogen under-potential deposition peaks measured in CV assuming a charge of 210 μC cm^{−2}_{Pt}, were 77 m² g^{−1}_{Pt} for CNT and 81 m² g^{−1}_{Pt} for conventional. The ECSAs were close and it was consistent with the fact that the Pt particle size of CNT and that of the conventional catalyst reported in literature [39] were also about 2.3 nm. And the each specific activity (SA) was 409 μA cm^{−2}_{Pt} and 251 μA cm^{−2}_{Pt}. Although Pt/CNT's MA and SA were about 1.5-fold higher than those of the Pt/C reference catalyst, which is close result to Ref. [22], it could be said the CNTs used in these experiments did not affect the Pt particles' catalytic activity enough to improve the cell performance, because the difference of activity; 1.5 times higher current density is converted to just 12 mV by the relation 70 mV dec^{−1}.

Fig. 9 presents the Tafel plots of the 20 cm² cell's IR corrected IV performance data that are same as displayed in Fig. 7. The MA data corrected using the Pt loading, oxygen partial pressure and Tafel slope line measured with the RDE were plotted. The difference

Table 4
Durability test conditions.

Cell temperature	70 °C
Anode gas	H ₂ , 1 N L min ^{−1}
Cathode gas	N ₂ , 2 N L min ^{−1}
Gas pressure	Ambient
Dew point	70 °C
Potential step	0.9 V (5 s) ⇌ 0.6 V (5 s)

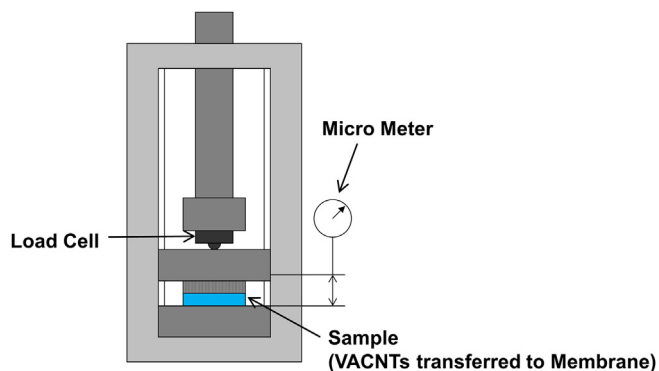


Fig. 5. Setup for stress-strain property measurement.

between MEA and RDE data, regarding to activity, was about 25 mV and close to that of conventional electrodes (not shown). It is reported that a difference of activity often observed related to the oxidation level of the Pt caused by difference of test conditions [38]. Under the single cell performance test condition, measuring sequence were 15 min for every points, the catalysts would be oxidized, compared to the RDE tests conducted under quicker cathodic potential sweep rate. The VACNT electrode's Tafel slope was consistently 70 mV dec^{−1} over a wide range below 1 A cm^{−2}. In case of the conventional electrodes, the absolute value of the Tafel slope frequently rise over 70 mV dec^{−1} in current density range of more than 0.1 A cm^{−2}, and the IR corrected potential passed below the 70 mV dec^{−1} line. Because an increased diffusion overpotential cannot be used at such low current density to explain this phenomenon, catalyst surface structure change models, such as Pt oxide formation [2,40] or sulfonic acid poisoning [41], were proposed. Our results did not exhibit a Tafel slope change at the low current density range with ordinary Pt catalysts, suggesting it was necessary to find a factor unrelated to the catalyst that explains the phenomenon of conventional MEAs.

Fig. 10 displays the limited current densities and the gas diffusion resistances calculated using Eq. (3), where R_{total} is the total gas diffusion resistance including data from the catalyst layer and GDL, P_{O_2} is the partial pressure of oxygen, R is the gas constant, T is temperature, F is faraday constant and i_{lim} is the limited current densities [34].

$$R_{\text{total}} = \frac{P_{\text{O}_2} 4F}{RT i_{\text{lim}}} \quad (3)$$

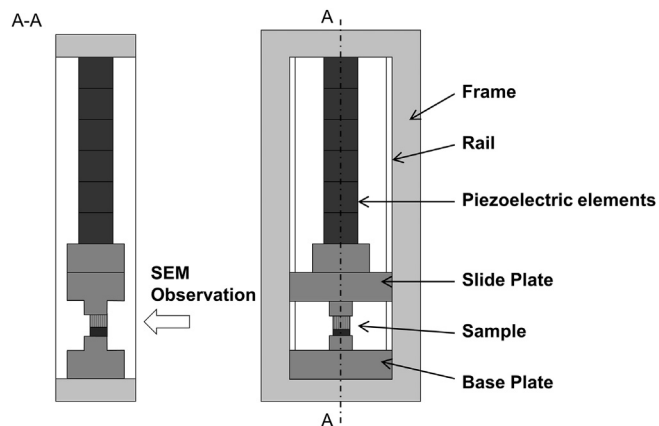


Fig. 6. Setup for in-situ SEM observation in compression test.

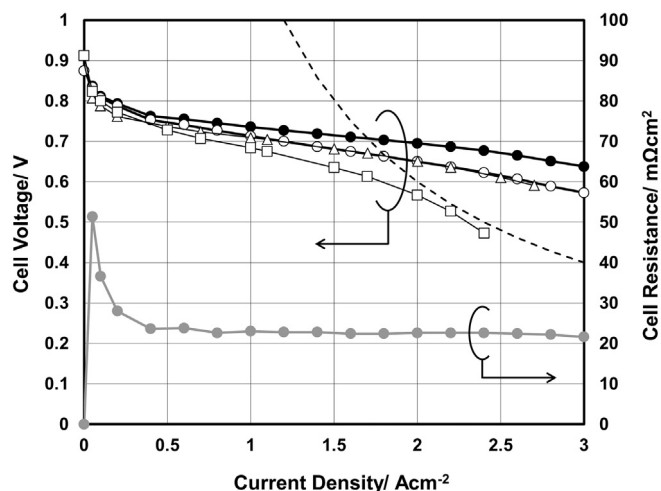


Fig. 7. IV performances of VACNT electrodes comparison to conventional electrode under test conditions shown in Table 3. ○: VACNT electrodes (20 cm² cell), ●: VACNT electrodes IR corrected (20 cm² cell), △: VACNT electrodes (236 cm² cell), □: conventional electrodes (236 cm² cell), ●: Cell resistance of VACNT electrodes. Dashed line: DOE target 0.125 g_{PGM} kW⁻¹.

In conventional electrodes, half of the total gas diffusion resistance was caused by the catalyst layer and the other half was generated by the GDL [4]. The VACNT electrodes' superior gas diffusivity was validated.

Although electrodes with high gas diffusivity often dry out easily, the data in Fig. 11 indicate that the VACNT electrodes worked well at high temperature dry conditions. This effect might be caused also by the good gas diffusivity. Two mechanisms for the potential drops during operation under dry conditions are possible: (1) Low ionomer hydration in the cathode catalyst layer causes low proton conductivity and concentrates the ORR reaction on the membrane side, increasing the overpotential, (2) Low ionomer hydration in the cathode catalyst layer decreases the oxygen gas diffusivity of ionomer covering the catalysts and increases the overpotential by low partial pressure of oxygen at the surface of the catalysts [42,43]. If mechanism (2) was dominant in VACNT

electrodes, then the results indicating that VACNT electrodes worked better in high temperature dry condition might be explained.

Fig. 12 presents the Pt dissolution durability test results. The ECSA drop rate for the VACNT electrodes equaled the drop rate for the conventional electrodes. However, decreases in the performance at high current densities were inhibited. The similar ECSA drop rates indicated, such as the RDE tests, that the Pt particles on the VACNT electrodes were not unique nor were they affected by the CNT supports. However, the high current density performance inhibition in the VACNT electrodes arose from their superior gas diffusivity. A similar mechanism was reported previously [2,4]; a low Pt loading (small ECSA) causes an increase in the activation overpotential and an increase in the concentration overpotential because the concentration of current per Pt surface area and the gas diffusivity resistance around the Pt particles, meaning within the ionomer, increases.

3.2. Morphology

The MEAs' compositional volume fractions after the cell performance tests were estimated as described in Fig. 13; the pore volume fractions of both the VACNTs and conventional electrode catalysts were similar. Using the high resolution cross-sectional SEM images of the electrodes (Fig. 14), large, continuous pores were observed in VACNT electrodes, while agglomerates larger than 100 nm were observed in conventional electrodes. Therefore, the VACNT electrodes' high gas diffusivity might be caused by the pore structure and not the pore volume ratio. Considering the volume of ionomer in electrodes, the absolute volume of ionomer, which was experimentally optimized, in VACNT electrodes was about 1.7 times larger than in conventional electrodes. On the assumption that ionomer covers the catalyst supports in same thickness after optimization, the content of ionomer will be proportional to the surface area of the supports. If the covered surface area of CNTs is equal to the geometrical surface area, i.e., outer wall of 20 nm diameter cylinder, the diameter of the supports in conventional electrodes, assumed sphere with 1/1.7 surface area, is 60 nm. This value is not so far from the diameter of the agglomerates shown in Fig. 14. After all, the lower ionomer content of conventional electrodes might suggest the presence of agglomerates. Anyway, while the quantitative measurement of the

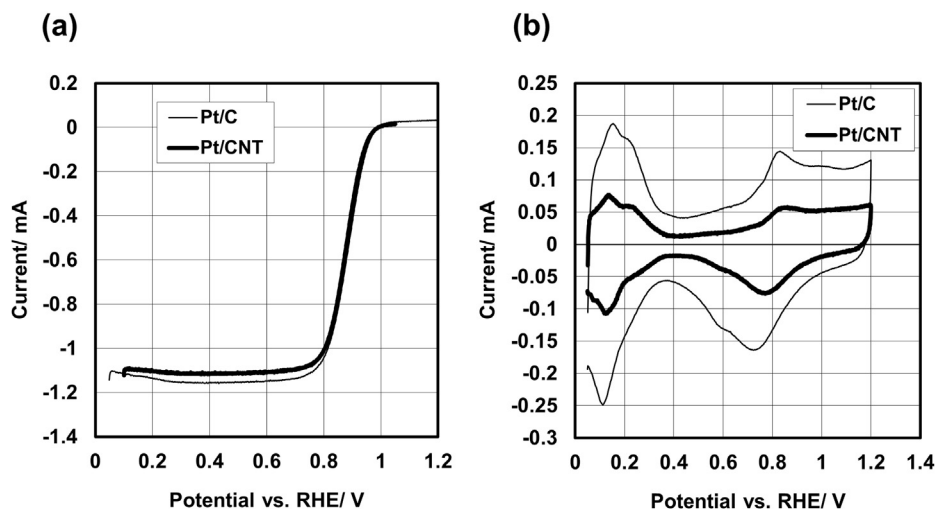


Fig. 8. a) Linear sweep voltammogram under oxygen saturated condition, b) cyclic voltammograms under argon saturated condition on Pt/CNT and Pt/Ketjen black by rotating disc electrode technique. 0.1 M HClO₄ solution, 25 °C, rotation rate 1600 rpm, scan rate 10 mV s⁻¹.

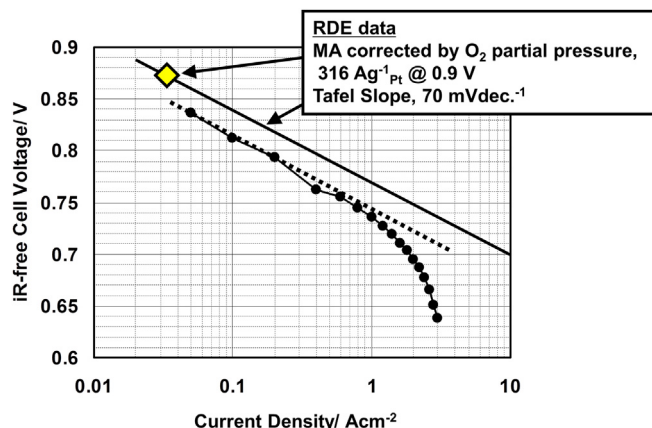


Fig. 9. Tafel plots of VACNT electrodes MEA (●: same data in Fig. 7) with mass activity data in Fig. 8 corrected by oxygen partial pressure.

electrodes' pore structure is necessary, it has not been achieved because the recently reported quantitative analyses, such as SEM tomography [44] or mercury intrusion porosimetry [45], were not applicable to VACNT electrodes. The resolution of SEM tomography was not high enough when low acceleration voltage was used to avoid damaging the ionomer. Mercury intrusion porosimetry has difficulty measuring the porosity of elastic materials, such as VACNTs.

In Fig. 14, the CNTs' vertical alignment directions are displayed together. At the microscopic level, the CNTs were no longer vertically aligned. Therefore, the vertical alignment property was critical to generate continuous pores during the MEA manufacturing process but was not crucial for the cell performance.

Fig. 15 presents the stress–strain characteristics of the VACNT electrode transferred membranes, and Video 1 displays a SEM video of VACNTs coated with ionomer under compression and release. Fig. 16 shows snapshots of VACNTs before and after compression. The VACNTs have elasticity similar to Ref. [23] except that their stress value was approximately one digit smaller because CNTs have a small diameter and numerical density. An elastic catalyst layer possesses two advantages. First, elasticity makes the thickness of the catalyst layer easy to control and optimize. Overly thick catalyst layers worsen the mass transport and excessively thin layers cause pore blockages, resulting in poor drainage and/or decreased robustness against temperature and humidity change. The optimized thickness for the VACNT electrodes was 6–8 μm ,

which is similar to the optimal thickness for the conventional electrodes. Second, the elasticity may ensure the contact between catalyst layer and microporous layer (MPL) occurs. When space exists in the interface, the residual water remaining does not drain easily because the water moves only from smaller to bigger pores; the driving force for water movement is the hydrophobicity of the pore surfaces. Good contact is very important, especially in the high current density regions that make more water. The MPL's surface roughness is usually higher than the roughness of the catalyst layer because MPL consists of a rougher material (GDL). To fully adhere two materials with different levels of surface roughness, the smoother material must be flexible enough to absorb the roughness of its counterpart. The flexible CNTs fill the space between the top of CNTs and the block pressing the CNTs. In addition, the VACNT electrodes were compressed after the cell tests and did not recover, as observed in Fig. 15 and Video 1. The difference is the presence of liquid water. The compression property tests (Fig. 15 and Video 1) were conducted under dry conditions to simulate the preparation processes; however, the electrodes in the cells were pressed under wet conditions. The ionomer partially solved this problem and worked as an adhesive.

Supplementary video related to this article can be found at <http://dx.doi.org/10.1016/j.jpowsour.2013.11.073>.

Although optimal structures of the VACNTs used for the electrodes in PEFCs have not been clarified, we would like to emphasize a superiority of the VACNTs usage for the electrodes. For the electric double-layer capacitor application, it is well-known that small diameter, long, high surface area, dense and highly packed CNTs are suitable and under development [26]. Now, we would like to summarize the prefer structure of the VACNTs for the electrodes. The requirements for the catalyst supports include sufficient surface area and anchoring sites to load the Pt nano particles. The following equation expresses the relationship between CNT structure and surface area.

$$\pi d h \tau \kappa n > s \rho \quad (4)$$

where d , h , τ , κ and n are the diameter, height, tortuosity, ratio of BET surface area by geometric surface area, and number density of the CNTs per electrode area, while s is the required BET surface area per unit Pt loading and ρ is the Pt loading per electrode area. The left side of the equation is geometric surface area of CNTs and the

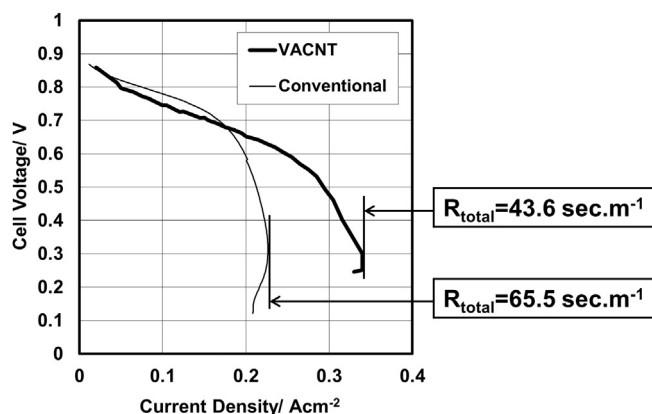


Fig. 10. Polarization curves of VACNT electrodes and conventional electrodes on limiting current density measurement under test conditions shown in Table 3.

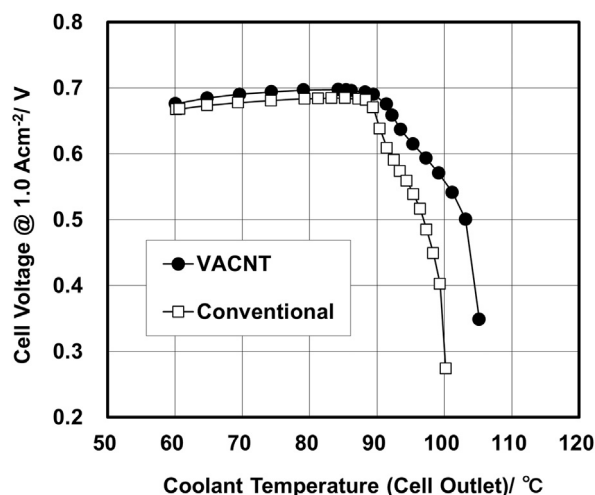


Fig. 11. Temperature dependence characteristics of VACNT electrodes MEA and conventional electrodes MEA under test conditions shown in Table 3.

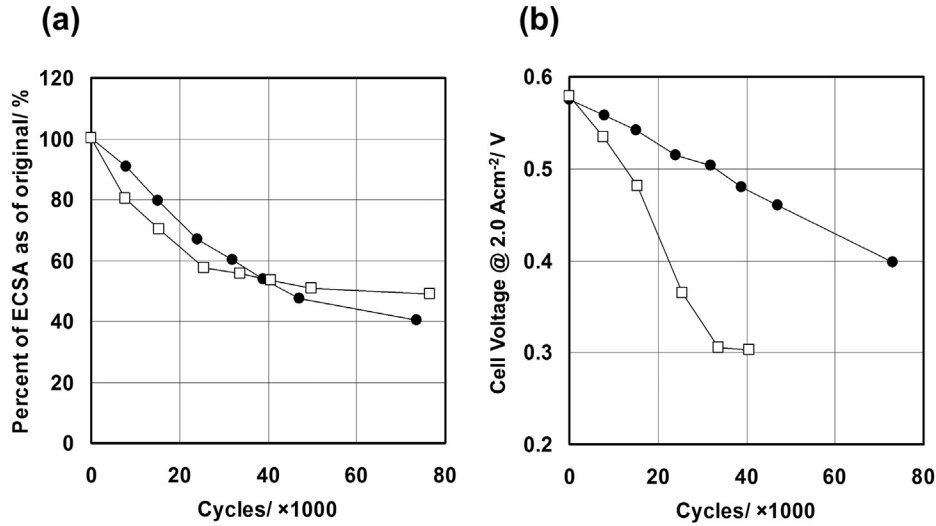


Fig. 12. Durability test results. a) ECSA loss rate and b) voltage loss of VACNT electrodes and conventional electrodes under test conditions shown in Table 3.

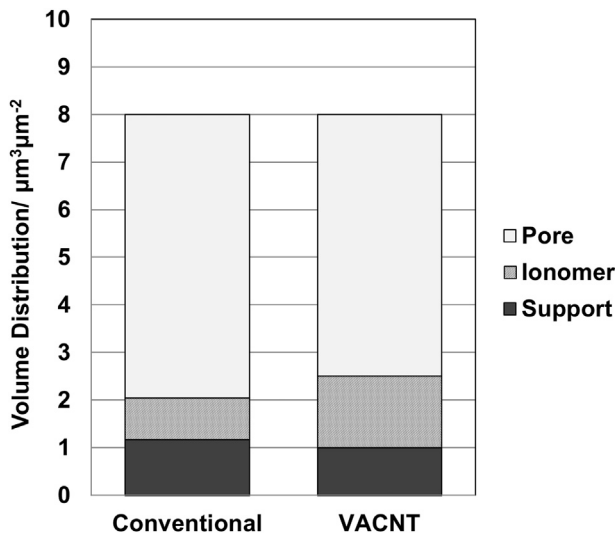


Fig. 13. Compositional volume fractions of electrodes.

right side is required surface area for Pt nano particles loading. Sufficient distance is also required for ionomer impregnation:

$$\frac{1}{\sqrt{n}} - d > D \quad (5)$$

where D is the distance required for ionomer colloid impregnation. The first term of left side is the distance from CNT center to center, assuming grid arrangement, and hole left side indicates the surface to surface distance of CNTs. Equations (4) and (5) should be satisfied to avoid process issues.

The pore continuity is important for mass transfer in electrodes, and when the same pore volumes as conventional electrodes are also necessary, the following equation is applicable:

$$t - \frac{\pi}{4} d^2 h \tau n - \frac{m}{\rho_l} > k \quad (6)$$

where t is electrode's thickness, m is the ionomer loading, ρ_l is the ionomer density and k is the required pore volume. The second term of left side is the volume of CNTs and the third term is the volume of ionomer. The left side of the equation indicating the vacancy of the electrodes, where the volume of Pt particles is ignored, should be larger than a required value for mass transfer.

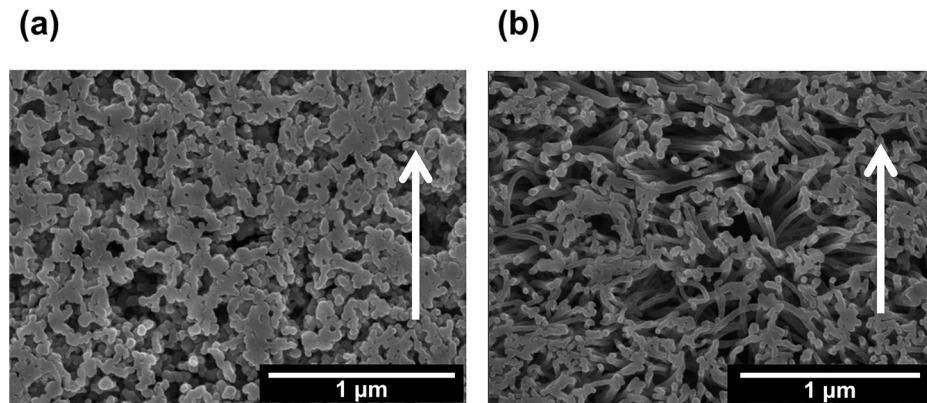


Fig. 14. Cross sectional SEM view of a) VACNT electrodes and b) conventional electrodes. White arrows indicate vertical direction.

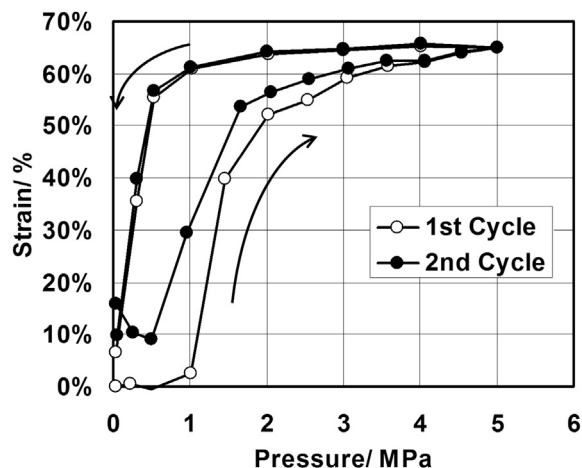


Fig. 15. Stress-strain characteristics of ionomer coated VACNT forest transferred to membrane.

Fig. 17 displays the area required for the VACNT structure (length, number density and diameter) as described by Equations (3)–(5), where $D = 150$ nm (experimental value in our process), $s = 467 \text{ m}^2 \text{ g}^{-1} \text{ Pt}$ (calculated from the $200 \text{ m}^2 \text{ g}^{-1}$ specific surface area and the 30 wt.% Pt loading density on the CNTs we used, which were similar to the Vulcan), $m = 0.3 \text{ mg cm}^{-2}$, $\rho_1 = 2 \text{ g cm}^{-3}$, $k = 4 \times 10^{-4} \text{ cm}^3 \text{ cm}^{-2}$ and $t = 8 \text{ }\mu\text{m}$. Boyer et al. noted that the maximum thickness of the electrodes was limited to 20–25 μm due to proton conductivity [46]. Considering the difference between their fully saturated test condition and our dry test condition (the relative humidity of the cathode inlet gas was 0% while the outlet gas humidity was 75% at low current density and 130% at high current density), as well as the relationship between relative humidity and the ionomer's proton conductivity [47], the average proton conductivity in our cells would be several times higher than that of fully saturated cells. The assumed 8 μm thickness, which was the experimentally optimized value (Section 2.1), might be reasonable for this estimation. In Fig. 17, the smaller diameter extends the acceptable lengths and number densities, because the CNTs with small diameter having larger specific surface area can reduce the CNTs' volume ratio and increase the pore volume

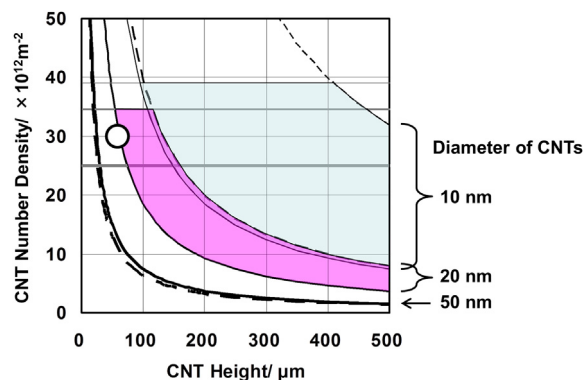


Fig. 17. Required area for VACNT structure of length, diameter and number density. Solid lines are lower limits of number density of CNTs for Pt loading, solid gray horizontal lines are upper limits for ionomer impregnation and dashed lines are upper limits for necessity for pore volume for each diameter of CNTs. Fine lines: 10 nm, middle lines: 20 nm, thick lines: 50 nm. \circ : current CNTs.

keeping enough surface area. There is no acceptable area when the CNTs have diameters larger than 50 μm . Furthermore, there is no permissible area on the line for CNTs 8 μm height, indicating the cells were not compressed. Specifically, before compressing the electrode to the appropriate thickness, impregnation of the CNT forests with ionomer colloids maintaining their vacancies larger than the ionomer colloids was indispensable.

4. Conclusion

We successfully developed cathode electrodes for PEMFC that enable high current density operation by incorporating VACNTs as a catalyst support. The current density at 0.6 V was 2.6 A cm^{-2} when the Pt loading was 0.1 mg cm^{-2} on the cathode; this value was achieved due to the improved mass transport. The mass transport improved due to the pore continuity, the non-agglomerating catalyst supports and the good electrical contact between the catalyst and microporous layers. However, the CNTs in the compressed cells were no longer vertically aligned; fortunately, the vertical alignment was important when creating the continuous pores and better ionomer coating during the MEA manufacturing

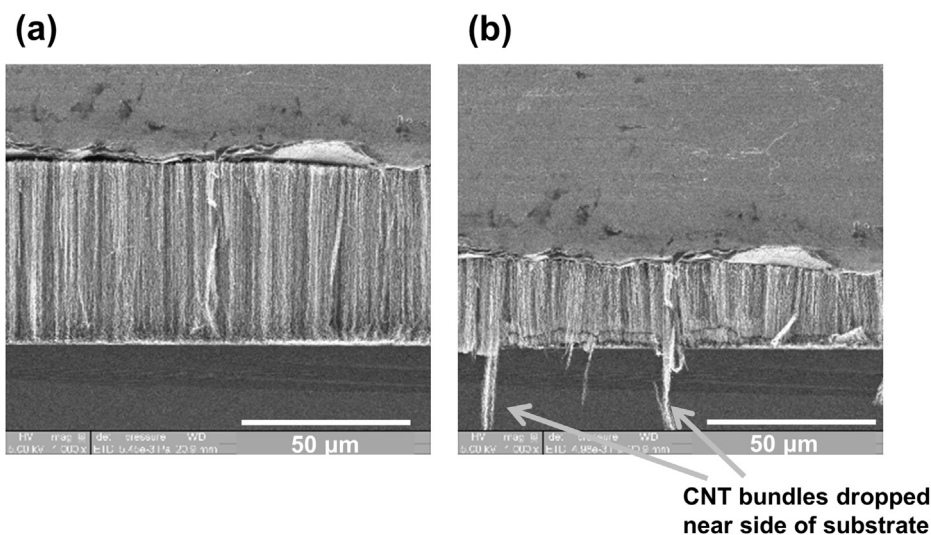


Fig. 16. SEM image of VACNT forest under compression. a) early stage in compression, b) final stage in compression.

process, but was not critical to the cell performance. The optimal VACNT structure was dictated by the process requirements and cell performance, featuring diameters less than 20 nm, while being taller than 50 μm with distances above 150 nm between the CNTs.

Acknowledgments

The authors would like to thank the Hitachi Zosen Corporation for developing and supplying the VACNTs optimized for the PEMFC electrodes. In addition, the authors are also grateful for the interesting SEM video provided by Dr. Takanao Tomura from Nippon Soken, Inc.

References

- [1] New Energy and Industrial Technology Development Organization (NEDO) Road Map of PEFC, <http://www.nedo.go.jp/content/100086290.pdf> (in Japanese).
- [2] A. Ohma, T. Mashio, K. Sato, H. Iden, Y. Ono, K. Sakai, K. Akizuki, S. Takaichi, K. Shinohara, *Electrochim. Acta* 56 (2011) 10832–10841.
- [3] A.K. Srouji, L.J. Zheng, R. Dross, A. Turhan, M.M. Mench, *J. Power Sources* 218 (2012) 341–347.
- [4] N. Nonoyama, S. Okazaki, A.Z. Weber, Y. Ikogi, T. Yoshida, *J. Electrochem. Soc.* 158 (2011) B416–B423.
- [5] M.S. Wilson, S. Gottesfeld, *J. Appl. Electrochem.* 22 (1992) 1–7.
- [6] M.K. Debe, Annual Progress Report, DOE Hydrogen and Fuel Cells Program, V. D. 1, 2011. http://www.hydrogen.energy.gov/pdfs/progress11/v_d_1_debe_2011.pdf.
- [7] B. Winther-Jensen, O. Winther-Jensen, M. Forsyth, D.R. MacFarlane, *Science* 321 (2008) 671–674.
- [8] J.B. Ballengee, P.N. Pintauro, *J. Electrochem. Soc.* 158 (5) (2011) B568–B572.
- [9] Y. Qiu, J. Yu, T. Shi, X. Zhou, X. Bai, J.Y. Huang, *J. Power Sources* 196 (2011) 9862–9867.
- [10] W. Mei, T. Fukazawa, T. Sato, Y. Nakano, US Patent 8128986.
- [11] W. Li, X. Wang, Z. Chen, M. Waje, Y. Yan, *Langmuir* 21 (2005) 9386–9389.
- [12] Jason M. Tang, Kurt Jensen, Mahesh Waje, Wenzhen Li, Paul Larsen, Kevin Pauley, Zhongwei Chen, Palanisamy Ramesh, Mikhail E. Itkis, Yushan Yan, Robert C. Haddon, *J. Phys. Chem. C* 111 (2007) 17901–17904.
- [13] W. Zhu, J.P. Zheng, R. Liang, B. Wang, C. Zhang, S. Walsh, G. Au, E.J. Plichta, *ECS Trans.* 16 (2) (2008) 1615–1626.
- [14] M. Lebert, M. Kaempgen, M. Soehn, T. Wirth, S. Roth, N. Nicoloso, *Catal. Today* 143 (2009) 64–68.
- [15] J. Yang, G. Goenaga, A. Call, D.-J. Liu, *Electrochem. Solid-State Lett.* 13 (6) (2010) B55–B57.
- [16] Y. Shao, G. Yin, Y. Gao, P. Shi, *J. Electrochem. Soc.* 153 (6) (2006) 1093–1097.
- [17] L. Li, Y. Xing, *J. Electrochem. Soc.* 153 (10) (2006) 1823–1828.
- [18] T. Hatanaka, T. Takeshita, H. Murata, N. Hasegawa, T. Asano, M. Kawasumi, Y. Morimoto, *ECS Trans.* 16 (2) (2008) 1961–1965.
- [19] M. Carmo, V.A. Paganin, J.M. Rosolen, E.R. Gonzalez, *J. Power Sources* 142 (2005) 169–176.
- [20] K.O. McElrath, K.A. Smith, J.L. Bahr, T.J. Wainerdi, D.A. Karohl, D.T. Colbert, M.A. Miller, H.W. Oviatt, E.D. Cline, US Patent US 20040197638A1.
- [21] G. Girishkumar, M. Rettker, R. Underhile, D. Binz, K. Vinodgopal, P. McGinn, P. Kamat, *Langmuir* 21 (2005) 8487–8494.
- [22] A. Kongkanand, S. Kuwabata, G. Girishkumar, P. Kamat, *Langmuir* 22 (2006) 2392–2396.
- [23] A. Cao, P.L. Dickrell, W.G. Sawyer, M.N. Ghasemi-Nejhad, P.M. Ajayan, *Science* 310 (2005) 1307–1310.
- [24] H. Nakanishi, K. Sekizawa, N. Kobayashi, K. Nakata, C. Inazumi, Y. Sairyo, D. Fujita, H. Shiozaki, Japan Patent 2005-4967 (in Japanese).
- [25] T. Hatanaka, H. Nakanishi, S. Matsumoto, Y. Morimoto, *ECS Trans.* 3 (1) (2006) 277–284.
- [26] D.N. Futaba, K. Hata, T. Yamada, T. Hiraoka, Y. Hayamizu, Y. Kakudate, O. Tanaike, H. Hatori, M. Yumura, S. Iijima, *Nat. Mater.* 5 (2006) 987–994.
- [27] J. Bult, A. Dameron, S. Pylypenko, C. Engtrakul, C. Bochet, L. Chen, G. Leong, S. Frisco, L. Simpson, H.N. Dinh, B. Pivovar, *ECS Trans.* 33 (1) (2010) 89–96.
- [28] K. Nishimura, N. Okazaki, L. Pan, Y. Nakayama, *Jpn. J. Appl. Phys.* 43 (2004) 471–474.
- [29] H. Shioyama, Y. Yamada, Y. Sairyo, *TANSO* 209 (2003) 171–173 (in Japanese).
- [30] Hitachi Zosen Corporation, News Release, Jan. 28, 2013. <http://www.hitachizosen.co.jp/english/release/2013/01/000850.html>.
- [31] P.A. Cirkel, T. Okada, S. Kinugasa, *Macromolecules* 32 (1999) 531–533.
- [32] C.-H. Ma, T.L. Yu, H.-L. Lin, Y.-T. Huang, Y.-L. Chen, U.-S. Jeng, Y.-H. Lai, Y.-S. Sun, *Polymer* 50 (2009) 1764–1777.
- [33] M. Mizuhata, K. Oguro, M. Oguri, K. Sasaki, T. Asaki, Japan Patent P3452096 (in Japanese).
- [34] D. Baker, C. Wieser, K.C. Neyerlin, M.W. Murphy, *ECS Trans.* 3 (1) (2006) 989–999.
- [35] Fuel Cell Commercialization Conference of Japan (FCCJ) Test Protocol, http://www.fccj.jp/pdf/23_01_kt.pdf (in Japanese).
- [36] DOE Fuel Cell Technologies Office Multi-year Research, Development and Demonstration Plan, 3.4 Fuel Cells, 2012, p. 27.
- [37] W. Vielstich, H. Gasteiger, A. Lamm (Eds.), *Handbook of Fuel Cells – Fundamentals, Technology and Applications*, vol. 2, Wiley, 2003, p. 316 (Chapter 22).
- [38] H. Gasteiger, S. Kocha, B. Sompalli, F. Wagner, *Appl. Catal. B: Environ.* 56 (2005) 9–35.
- [39] M. Heggen, M. Oezaslan, L. Houben, P. Strasser, *J. Phys. Chem. C* 116 (2012) 19073–19083.
- [40] N.P. Subramanian, T.A. Greszler, J. Zhang, W. Gu, R. Makharia, *J. Electrochem. Soc.* 159 (5) (2012) B531–B540.
- [41] R. Subbaraman, D. Strmcnik, A.P. Paulikas, V.R. Stamenkovic, N.M. Markovic, *Chem. Phys. Chem.* 11 (13) (2010) 2825–2833.
- [42] H. Xu, H. Russell Kunz, J.M. Fenton, *Electrochim. Acta* 52 (2007) 3525–3533.
- [43] A.A. Kulikovskiy, *Electrochem. Commun.* 13 (2011) 1395–1399.
- [44] V. Berejnov, D. Susac, J. Stumper, A.P. Hitchcock, *ECS Trans.* 50 (2) (2013) 361–368.
- [45] Z. Yu, R.N. Carter, *ECS Trans.* 19 (17) (2009) 1–15.
- [46] C. Boyer, S. Gamburg, O. Velez, S. Srinivasan, A.J. Appleby, *Electrochim. Acta* 43 (1998) 3703–3709.
- [47] Y. Sone, P. Ekdunge, D. Simonsson, *J. Electrochem. Soc.* 143 (1996) 1254–1259.